Eulerian-Lagrangian CFD Model for Prediction of Heat Transfer between Aircraft Deicing Liquid Sprays and a Surface

Sami Ernez and François Morency

Department of Mechanical Engineering
École de technologie supérieure
Montréal, Québec, Canada
Email:sami.ernez.1@etsmtl.net

Abstract

Purpose – This paper presents a Eulerian-Lagrangian model of aircraft ground deicing that avoids the scale dispersion problem caused by the considerable distance between the spray nozzle and the surface to be de-iced. Verification is done using the case of a hot particle liquid spray impinging on a horizontal flat plate. The impinged particles flow outwards radially from the impingement zone and form a hot film wall. The computed wall heat distribution is verified. In the end, an inclination spray angle study is presented.

Design/methodology/approach – The problem is divided into two regions. First, a 3D region is created for the evolution of the Lagrangian particle spray. A second 2D region is provided for the formation of a liquid film. The two regions exchange mass, momentum, and energy through an interface. Heat losses are modelled through particles and liquid film cooling and evaporation, particle splash, and heat transfer to a fixed temperature plate.

Findings – spray penetrations are in agreement with 10% of experiment when it is injected in a pressure of 1 bar. For this case study, the heat transfer is maximized when the inclination angle is close to 30° of the spray.

Originality/value – The model presented makes it possible to simulate the impingement and heat transfer of a large-scale liquid spray at reasonable computational cost. This model is a first attempt at the CFD simulation of ground deicing.

Keywords Liquid spray impingement, two-region Eulerian-Lagrangian model, heat transfer.

Paper type Research paper

Nomenclature

A_{wall}	Cell surface (m^2)	C_d	Drag coefficient of a sphere
D	Nozzle diameter (m)	$\bar{d}$	Particle characteristic diameter (m)
D_k	Diffusion coefficient of the k species (m$^2.s^{-1}$)	d_p	Particle diameter (m)
$\mathbf{F_{drag}}$	Spherical drag force (N)	$\mathbf{g}$	Gravitational acceleration (m.s^{-2})
H	Nozzle-surface distance (m)	h	Enthalpy of the internal field (w.s.kg^{-1})
h_F	Enthalpy of the liquid film (w.s.kg^{-1})	htc_p	Patch convective heat transfer coefficient (w.m^{-2}K^{-1})
k	Turbulence kinetic energy (m$^2.s^{-2}$)	n	Particles size distribution parameter
m	Mass (kg)	Nu_0	Nusselt number at the stagnation point
N_x	Characteristic cells number	$P_{a,n}$	Number of absorbed particles at nth time step
Nu	Nusselt number	$P_{s,n}$	Number of splashed particles at nth time step
p	Pressure field (Pa)	Pr	Prandtl number
$P_{inj,n}$	Number of injected particles at nth time step	Q_{evap}	Evaporation energy source term (W.m^{-2})

Symbol	Definition	Symbol	Definition
P_n	Total number of particles at n^{th} time step	Q_{imp}	Impingement energy source term (W.m^{-2})
Pr_t	Turbulent Prandtl number	$q_w^{"}$	Wall convective heat flux (W/m²)
$q_g^{"}$	Gas convective heat flux (W.m^{-2})	Re_D	Reynolds number based on nozzle diameter
Q_{spl}	Splashing droplet energy source term (W.m^{-2})	$S_{i,p}$	Momentum exchanged with particles (kg.$m^{-2}s^{-1}$)
r	Distance to the stagnation point (m)	$S_{\rho\delta}$	Surface flux density source term (kg.m^{-2})
Re_F	Wall film region Reynolds number	t	Physical time (s)
S_{c_k}	Schmidt number of the k species	T	Temperature (K)
$S_{\rho\delta u}$	Tangential momentum of surface source term (kg.$m^{-1}s^{-1}$)	$\mathbf{u}$	Internal field velocity (m.s^{-1})
T^*	Dimensionless temperature	$\mathbf{u_F}$	Wall film velocity (m.s^{-1})
$u_{i(i=1,2,3)}$	Component of $\mathbf{u}$ in a Cartesian reference	$x_{i(i=1,2,3)}$	Components in a Cartesian reference (m)
$\mathbf{u_P}$	Particle velocity (m.)	z	Wall film normal direction
Y_k	Mass fraction of species k	δ	Liquid film thickness (m)
α_t	Turbulent thermal diffusivity	Δz_F	Wall film region thickness (m)
ε	Rate of dissipation of turbulence energy (m² . s^{-3})	$\kappa = 0.41$	Von Kármán constant
θ	Spray inclination angle (rad)	μ	Internal field dynamic viscosity (N.s.m^{-2})
κ_p	Thermal conductivity (w.$M^{-1}.K^{-1}$)	ν_t	Turbulent kinematic viscosity (m².s^{-1})
μ_F	Liquid film dynamic viscosity (n.s.M^{-2})	ρ_p	Particle density (kg.m^{-3})
ρ	Internal field density (kg.m^{-3})	$\mathbf{\tau_{eff}}$	Effective shear tensor
$\mathbf{\tau}$	Internal field shear stress (N.m^{-2})	$\dot{\omega}_i$	Source term describing the generation or destruction of a species (kg.$m^{-3}s^{-1}$)
$\mathbf{\tau_F}$	Wall film shear stress (N.m^{-2})	ρ_F	Wall film region density (kg.m^{-3})

Introduction

In Northern countries, aircraft icing can occur on the ground due to climatic conditions. Ice affects the aerodynamic properties of aircraft and makes their take-off difficult or even impossible. Following several crashes during take-off (Moshansky, 1992; National Transportation Safety Board, 1993), Canada instituted regulations forbidding any plane with frosted surfaces from taking off, and requiring that such aircraft be immediately deiced. North American standards require that deicing operations be carried out using a hot impinging spray of aircraft deicing fluid (ADF). Transport Canada acknowledges only the most up-to-date SAE specifications, and all fluids applied to aircraft must meet these high standards (Transport Canada, 2005). ADFs are highly miscible with water, and consequently, deicing fluid that flows onto the tarmac contaminates effluents and seeps into underground soils. In 2005, to limit the polluting effects of aircraft deicing, the Canadian Council of Ministers of the Environment prepared water quality guidelines for airports meeting Canada-specific conditions (Transport Canada, 2005). Pursuant to those guidelines, de-icers must either recover or recycle ADFs. However, this additional operation increases ground deicing costs for aircraft. It is therefore evident that reducing the volume of ADF needed to de-ice an aircraft carried both environmental and economic benefits.

The preheated ADF is sprayed directly onto the contaminated surface. Transport Canada also recommends that the fluid be dispensed as close to the surface as possible to prevent it from cooling down. Further, it should be applied at a particular angle to avoid damaging the aircraft surface (Transport Canada, 2005). To date, no parametric studies on aircraft ground deicing have investigated the impingement distance and the liquid spray angle effects on melting an iced surface.

Today, CFD codes are commonly used to predict in-flight aircraft icing accretion (Beaugendre, Morency and Habashi, 2006). CFD has proved useful in the prediction of the super-cooled droplet impingement area (Bilodeau et al., 2016) and in the design of de-icing and anti-icing systems (Wong, Papadakis and Wong, 2013; Pourbagian and Habashi, 2015). An in-flight icing model can use a Eulerian or a Lagrangian model for the droplet motion, loosely coupled with airflow and a 2D water film region on the aircraft surface. For deicing liquid spray, however, the airflow is driven by the warm droplet, and must be tightly coupled to the droplet motion. For aircraft in-flight icing, the droplet concentration is relatively low (Bourgault et al., 1999), and droplets come from a large area in front of the aircraft. On the ground, the droplets come from a known small area and are highly concentrated. On the aircraft surface, instead of accreting ice, the film flow melts the existing ice. In-flight thermal deicing involves heat transfer from the surface toward the external flow (Reid et al., 2010), while ground deicing involves heat transfer from the external flow toward the surface.

Similar for in-flight icing, CFD models could provide useful information to help improve ground de-icing activities. Yakhya, Ernez and Morency (2019) is the only study in literature that aims to model the aircraft ground deicing by CFD. It presents an impinging spray model coupled to a film model using volume of fluid method. However, the proposed problem is characterised by a large dispersion of the geometric length scales: a distance of 5D between the spray injection and the wall (sufficient at this verification step), a particle diameter of around D/100 and an average film thickness of D/25. The simulation of the liquid spray break-up into particles with a Eulerian method like volume of fluid or level set require a very high number of cells. These approaches focus on tracking the free boundary evolution. In this context , the free boundary should be drawn on several cells (Desjardins, Moureau and Pitsch, 2008; Shinjo and Umemura, 2010). Cell sizes should be smaller than droplets, which will lead to a very fine mesh. Given this constraint, a CFD bench test of aircraft ground deicing should not model the spray primary break-up. Rather, it should start with a droplet distribution modelling the spray behaviour just at the exit of the nozzle and model it as a particulate two-phase flow.

Here, two approaches are possible: a Eulerian approach and a Lagrangian approach. Durst, Milojevic and Schönung (1984) discussed the basic equations of the two approaches and their numerical treatment for a 2D vertical pipe case. They found that the Lagrangian approach is more appropriate for polydispersed particle size distributions. The Eulerian approach is more appropriate for flows with high particle concentrations. (Zhang and Chen, 2007) compared the modeling performance of the two approaches. They studied steady-state particle dispersion in a clean room and unsteady particle dispersion in a section of an aircraft cabin with a coughing passenger. They concluded that the Eulerian approach is efficient for steady-state calculations while the Lagrangian approach performed better in unsteady-state conditions. Fotovat, Bi and Grace (2017) reviewed the characterization methods of electrostatics and the mechanisms of charge generation and distribution in fluidized beds. Similar to Durst, Milojevic and Schönung (1984), they concluded that the Lagrangian approach is more appropriate for polydispersed particle size distributions. This paper proposes a 3D CFD model for predicting convective heat transfer in aircraft ground deicing process. The liquid spray is composed of polydispersed particle size. The process is modeled under unsteady-state conditions and given the large dimensions of the computation domain compared to the impinging jet sizes, low void fractions will be obtained. The Lagrangian approach is therefore favored in this work.

Combustion is surely the area that most solicits research to study liquid sprays and their interaction with a solid surface. The Lagrangian approach was used in many works. The interaction of the spray with a wall produce a wall film. In (Habchi et al., 1999) , the liquid film mass is tracked in a Volume of Fluid (VOF) framework. A Lagrangian method to track the liquid film also exists (Zhao et al., 2018, 2017). The Lagrangian method is more effective in combustion since the liquid film is considered as a dispersed phase. Another research field where impinging sprays were investigated is the spray quenching process. A Eulerian spray model interacting with a film model was used in (Edelbauer et al., 2016) to investigate the heat transfer with a preheated solid. The liquid film does evaporate because of the high temperature of the solid. In the quenching process, the film mass does not decrease as much as in combustion and a spray deposited film is created. The Eulerian representation of the film model is more adequate here since the liquid is considered as a continuous phase. In aircraft ground deicing the liquid film formed gain mass at each time step while it's fed by the spray and also the ice melting. Similar to (Yakhya, Ernez and Morency, 2019) the VOF method for the film modeling is then more interesting in the proposed case study. Given the proposed model constrains, the impinging spray model with Lagrangian particles and Eulerian film is superior to other impinging spray models.

The present paper aims to identify critical parameters of the liquid spray and evaluate its optimum value in order to reduce the volumes of ADF used to de-ice aircrafts. The main objectives of this research are to:
• Design a CFD bench test of aircraft ground deicing process on OpenFOAM;
• Correlate the ice mass removed by volume of ADF with spray parameters.

Velraj et al. (1999) demonstrated that convection is the dominant heat transfer mode in ice melting. ADF sprays remove ice by weakening and melting it under the effect of pressure and heat transfer. The specific objective of this paper is to propose a model that enables the CFD investigation of the convective heat transfer in deicing operations. Convective heat transfer predictions provide a basis for comparison between different deicing scenarios. The spray is modeled as a cloud of Lagrangian particles that impact an iced wall. The particles feed a Eulerian fluid film with momentum and heat.

No experimental data are available in literature to evaluate if breakup occur or not during the aircraft ground deicing process. However, the Akron Brass Company, (2019) proposes nozzles for de-icing with a wide range of choices in terms of injection pressure from 6 to 75 bar. Chigier and Reitz, (1996) reported that nozzle design effects are important for spray breakup. Varying the injection pressure with a constant mass flow rate will influence the Weber number which according to (Chigier and Reitz, 1996) determine if breakup occur or not. One direct effect of spray breakup is to have smaller droplets that increase heat and mass transfer surface. For aircraft de-icing, the cool down of the spray with distance is an important feature and break-up should be included in the model.

OpenFOAM provides a transient solver called reactingParcelFoam for compressible, turbulent flow with a reacting, multiphase particle clouds, and surface film modeling (Holzmann, 2016). The original solver was developed to model the particle deposition on a surface. It also handles chemical reactions and combustion. (Kampili, 2017) implemented a decay heat model and simulated nuclear aerosol transport. This solver models Lagrangian particles interaction with a Eulerian film model. However, it not handles particles breakup. We propose to add aircraft ground deicing to open a new application field for this solver. In this paper, we present the particles breakup model implementation in this solver. To do so, the ReactingCloud class was replaced by the SprayCloud class that enable breakup. The combustion module was also deleted for calculation efficiency. The model implementation is validated against spray tip penetration. For the verification of the new solver capabilities for ground aircraft de-icing simulations, the effect of droplet size on the wall heat transfer is investigated in this work.

The next section defines the impinging particle spray problem presented in the context of aircraft ground deicing. Section 3 demonstrates the mathematical model of the Lagrangian spray and the liquid film. Section 4 explains all the numerical schemes and describes the solver structure. Section 5 is dedicated to the model verification and a first validation step. Finally, a study on spray's inclination is shown at the end of the paper.

Problem definition

In the aircraft ground deicing process, an operator equipped with a special deicing vehicle directs the deicing nozzle toward the surface to be decontaminated. The ADF, heated to a specific temperature, is sprayed on the contaminated parts of the aircraft surface. The spray forms, in contact with ice, a liquid film flowing along the surface. Figure 1 shows a simplified scheme of the problem versus the real system.
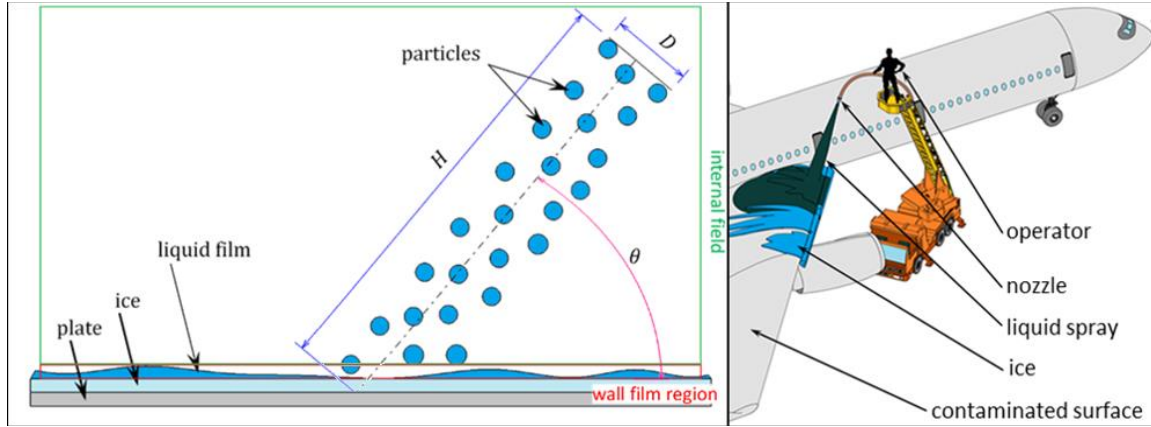
Figure 1: Simplified versus real scheme of aircraft ground de-icing process

In this study, the flow from the nozzle exit to the contaminated surface is modeled. The ice melting is not modeled. The nozzle exit position is fixed in time, contrary to the reality where the nozzle position changes in time. The proposed work aims to model the spray propagation from the nozzle exit until his impact on the surface using a Euler-Lagrange approach and a two-way coupling. A discoid particle source is placed inside the domain to model the spray at the nozzle's exit level. Particles may break up in the air and splash upon impinging the contaminated surface. The air is initially at rest, and the surface is at the air temperature. As the latent energy of the surface is high, the plate temperature is constant. For this paper, the plate and the ice volume are excluded from the computation domain, but the water film is included. The spray impinges a flat plate representative of a contaminated surface. The spray particle impacts a surface contaminated by frost. Upon impact, the particles enter the wall film region and create a liquid film. The liquid film flows over the surface, exchanges heat with ice and falls to the ground. In this article, the ability of a model to predict the heat transfer between a hot Lagrangian particle spray and a cold surface is investigated. The ice is not yet included; verification and validation of the Eulerian-Lagrangian model should be done first.

Mathematical model

This section describes the mathematical model of the problem. It is divided into three paragraphs. The first presents the gas phase equations that will be solved in a 3D mesh called here the internal field. The second paragraph briefly describes the Lagrangian particle model. The last paragraph describes the liquid film model for the surface flow. These equations will be resolved in a 2D domain called the *wall film region*.

In terms of object-oriented programming, 3 classes are created in OpenFOAM: *internalField*, *sprayCloud* and *wallFilmRegion*. Those classes exchange mass, momentum and energy. The figure below summarises the physical phenomena that are responsible for these exchanges. Particle and film evaporation generate a source term in the internal field continuity equation. The drag force exerted by the gas on particles disturbs the internal field velocity. For the energy balance, convective heat fluxes are modelled at the particle and film surfaces. The particles impacting and splashing on the film generate three source terms in the wall film region's governing equations.
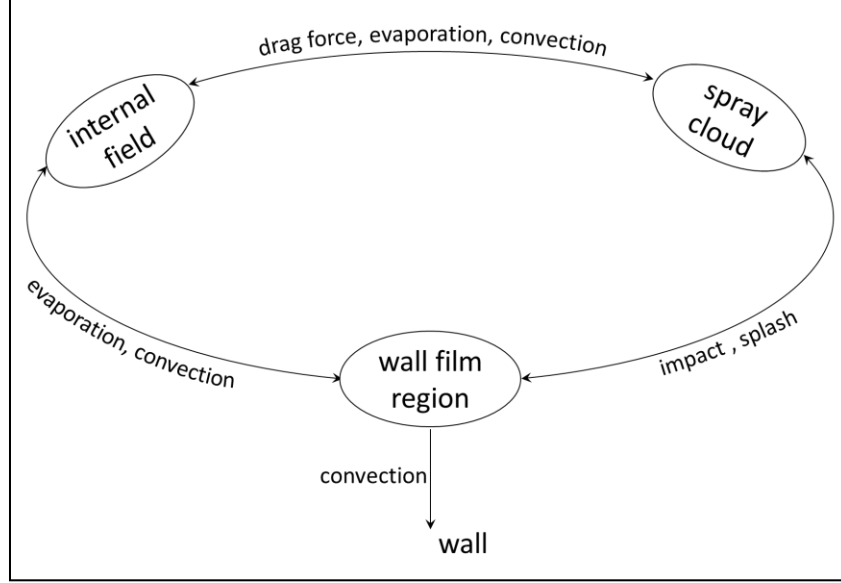
Figure 2: Physical phenomena linking particles, liquid film and gaseous phase

Internal field

The mass conservation (continuity) equation of sprayFilmFoam is given by the following equation:

$$\frac{\partial \rho}{\partial t} + \nabla.(\rho \mathbf{u}) = \dot{S}_{\rho,I \leftrightarrow P} + \dot{S}_{\rho,I \leftrightarrow F} \tag{1}$$

where $\dot{S}_{\rho,I \leftrightarrow P}$ and $\dot{S}_{\rho,I \leftrightarrow F}$ are mass source terms due to the evaporation of spray particles and liquid film, respectively.

$$\dot{S}_{\rho,I \leftrightarrow P} + \dot{S}_{\rho,I \leftrightarrow F} = \frac{\dot{m}_{F,evap} + \dot{m}_{P,evap}}{V_{Cell}} \tag{1.a}$$

The momentum conservation is given by the following equation:

$$\frac{\partial \rho \mathbf{u}}{\partial t} + \nabla.(\rho \mathbf{u}\mathbf{u}) = -\nabla p + \rho \mathbf{g} + \nabla.\left(2\mu_{eff}D(\mathbf{u})\right) - \nabla\left(\frac{2}{3}\mu_{eff}\nabla(u)\right) + \dot{S}_{u,I \leftrightarrow P} \tag{2}$$

where the effective viscosity μ_{eff} is the sum of the molecular and turbulent viscosity and the rate of strain (deformation) tensor $D(\mathbf{u})$ is defined as $D(\mathbf{u}) = \frac{1}{2}(\nabla \mathbf{u} + (\nabla \mathbf{u})^T)$. The pressure gradient and gravity force terms are rearranged numerically in the following form: $-\nabla p + \rho \mathbf{g} = -\nabla p_{rgh} - (\mathbf{g}.\mathbf{r})\nabla\rho$, where $p_{rgh} = p - \rho \mathbf{g} \cdot \mathbf{r}$ and $\mathbf{r}$ is the position vector from the wall. $\dot{S}_{u,p}$ is a momentum source term due to the drag force exerted by the fluid (ambient air) on liquid particles. The effect of the liquid film flow on the internal field is neglected.

The internal field is designed to initially have a chemical composition similar to the atmosphere. The evaporation of spray particles and fluid film introduces a third gaseous species. Aircraft deicing is carried out with an ADF spray. To be aligned with the literature, verifications are carried out using a water spray instead of ADF, so the third species will be noted here by the symbol X. These three gaseous entities are modelled by their mass fraction Y_k (gaseous), and are calculated from the equation of species in the internal field.

$$\frac{\partial \rho Y_k}{\partial t} + \nabla.(\rho Y_k \mathbf{u_F}) = \nabla.(\rho D_k \nabla Y_k) + \dot{\omega}_k \tag{3}$$

with D_k being a diffusion coefficient of the k species and $\dot{\omega}_k$ a source term describing the generation of a species. The spray and the liquid film contain only the X species, so $\dot{\omega}_{N_2} = \dot{\omega}_{O_2} = 0$ and $\dot{\omega}_{H_2O} = V_{evap}/V_{cell}$.

Energy conservation is ensured by solving the following enthalpy equation:

$$\frac{\partial \rho h}{\partial t} + \nabla.(\rho h \mathbf{u}) + \frac{\partial \rho K}{\partial t} + \nabla.(\rho K \mathbf{u}) - \frac{\partial p}{\partial t} = \nabla.(\alpha_{eff}\nabla h) + \rho \mathbf{u} \cdot \mathbf{g} + \dot{S}_{h,I \leftrightarrow P} + \dot{S}_{h,I \leftrightarrow F} \tag{4}$$

where $K \equiv \|\mathbf{u}\|^2/2$ is the kinetic energy per unit mass, h the enthalpy per unit mass, and α_{eff} is the effective thermal diffusivity, which is the sum of laminar and turbulent thermal diffusivities:

$$h = h_s + \sum_i c_i \Delta h_f^k \tag{4.a}$$

$$\alpha_{eff} = \frac{\mu}{Pr} + \frac{\rho \nu_t}{Pr_t} = \frac{\kappa_p}{\rho c_p} + \frac{\rho \nu_t}{Pr_t} \tag{4.b}$$

where $h_s = c_p T$ is the sensible enthalpy, c_k and Δh_f^k are respectively the molar fraction and the standard enthalpy of formation of the k species. κ_p is the thermal conductivity, c_p is the specific heat at constant pressure, μ is the dynamic viscosity, ν_t is the turbulent (kinematic) viscosity, Pr is the Prandtl number and Pr_t is the turbulent Prandtl number. $\dot{S}_{h,I\leftrightarrow P}$ models the particle evaporation and heat convection, and $\dot{S}_{h,I\leftrightarrow F}$ models the same phenomena at the liquid film level.

Spray cloud
The cylindric Lagrangian spray injector is specified by diameter, direction, velocity, mass flow, number of parcels per second and the droplet properties, namely, the temperature, the droplet diameter distribution and the mixture composition. The droplet size distribution injected is poly-dispersed. Poly-dispersed distributions are generally closer to the experimentally observed distribution of the sprays than their mono-dispersed counterparts. They are often specified using a normal, log-normal, or Rosin-Rammler distribution (Nasr, Yule and Bendig, 2002). In OpenFOAM, the distribution can also be specified as a user-defined probability density function or as a cumulative density function table for mass, volume or number of droplets. In this paper, the Rosin-Rammler mass distribution is used to describe the mass distribution of particles as a function of diameter. The description of this distribution can be found in Yoon et al. (2004).

The particle locations and speeds are obtained from Newton's second law. Particles are subjected to the gravity and drag $\mathbf{F}_{drag}$ forces. Different models of drag coefficients are available in the literature depending on particle sphericity. For example, Liu, Mather and Reitz (2010) developed a diesel engine spray model in which the particle drag coefficient changes dynamically with flow conditions during the particle's lifetime. This model gave better results than the commonly used rigid sphere drag coefficient model. However, the dynamic drag coefficient involves a particle distortion as another additional parameter. Liu, Mather and Reitz (2010) found that changing the drag coefficient from a rigid sphere model to a dynamic model has relatively little effect on spray penetration, and does influence the distribution of particle sizes within the spray. So, given the difference between the two applications and for the sake of simplicity, the common rigid sphere drag coefficient (Stiesch, 2003) is used in this work:

$$\mathbf{F}_{drag} = \frac{3}{4} \frac{\rho m_P}{\rho_P d_p} C_D (\mathbf{u} - \mathbf{u_P}) |\mathbf{u} - \mathbf{u_P}| \tag{5}$$

$$C_D = \begin{cases} \dfrac{24}{Re_p}\left(1 + \dfrac{1}{6} Re_p^{\frac{2}{3}}\right) & Re_p \leq 1000 \\ 0.424 & Re_p > 1000 \end{cases} \quad ; \quad Re_p = \frac{\rho}{\mu}.d_p.\|\mathbf{u} - \mathbf{u_p}\| \tag{5.a}$$

The momentum transfer between particles and the wall film region is modelled by adding the impacting particles' linear momentum to the thin film momentum equation (Stanton and Rutland, 1998; Meredith, 2010). Finally, the particle evaporation is modelled. The main assumptions are: (i) negligible effects of internal particle circulation and (ii) infinitely high diffusivity. For the sake of brevity, equations can be found in Nobile (2015).

Wall film region
The thin liquid film adheres to the contaminated plate. The thin liquid film model is based on two approximations: i) the film velocity in the normal direction of the adherence surface is assumed to be zero, and ii) the gradient of a variable in a collinear direction to the adherence surface is negligible compared to the gradient of the same variable in the direction normal to the surface. This means that thermal conduction and shear stress are dominant in the normal direction of the adherence surface. The liquid film is characterised by a thickness δ. Initially, the contaminated surface is supposed to be dry, i.e., it has a zero-film thickness. This

thickness varies due to the mass transfer with the liquid spray. The particle mass, moment and thermal energy that leave the internal field and head towards the wall film region are added as source terms in the liquid film conservation equations. As they enter the wall film region, the particles become a continuous mass uniformly distributed in the mesh cells. Any surface tension effects are neglected in the film model. The film thickness δ is calculated by solving the continuity equation at the film level (Stanton and Rutland, 1998; Meredith, 2010):

$$\frac{\partial \rho_F \delta}{\partial t} + \nabla_s . (\rho_F \delta \mathbf{u_F}) = \dot{S}_{\rho,P \leftrightarrow F} + \dot{S}_{\rho,F \leftrightarrow I} \tag{6}$$

$$\dot{S}_{\rho,F \leftrightarrow P} + \dot{S}_{\rho,F \leftrightarrow I} = \frac{\dot{m}_{F,evap} + \dot{m}_{imp} + \dot{m}_{spl}}{S_{Cell}} \tag{6.a}$$

∇_s is the 2D differential operator in the two directions tangential to the wall film region. $\mathbf{u}_F$ is the average film velocity in the normal direction of the film. $\dot{S}_{\rho,P \leftrightarrow F}$ is a source term that models the variation of the film mass flow rate due to the impact and splashing particles and film evaporation. The mass flow rate of the impacting particles $\dot{m}_{imp}$ is provided by the resolution of the Lagrangian particle's equation of motion in the internal flow region.

The momentum conservation in the wall film region is given by the following equation:

$$\frac{\partial \rho_F \delta \mathbf{u_F}}{\partial t} + \nabla_s . (\rho_F \delta \mathbf{u_F} \mathbf{u_F}) = -\delta \nabla_s(p) + \rho_F \mathbf{g} \delta + \frac{\tau_F}{A_{wall}} - \dot{\mathbf{S}}_{u,P \leftrightarrow F} \tag{7}$$

with

$$\dot{\mathbf{S}}_{u,F \leftrightarrow P} = \frac{\dot{M}_{tang}}{A_{wall}} = \frac{\dot{m}_{P_{impact}} \mathbf{u_{imp}} - \dot{m}_{splash} \mathbf{u_{spl}}}{A_{wall}} \tag{7.a}$$

$$\tau_F = \tau_{wall} + \bar{\tau} = \mu \left(\frac{\partial \mathbf{u_F}}{\partial z}\right)_{z=0} + \mu \left(\frac{\partial \mathbf{u_F}}{\partial z}\right)_{z=\delta} \tag{7.b}$$

The film enthalpy is calculated from the energy equation neglecting the radiation term (Stanton and Rutland, 1998; Meredith, 2010):

$$\frac{\partial \rho \delta h_F}{\partial t} + \nabla_s . (\rho \delta \mathbf{u_F}) h_F = q_w(h_{F,s}) + \dot{S}_{h,F \leftrightarrow P} + \dot{S}_{h,F \leftrightarrow I} \tag{8}$$

where h_F is the enthalpy averaged in the film normal direction. $h_{F,s}$ is the film sensible enthalpy, $q(h_{F,s})$ is the film heat flux. $\dot{S}_{h,F \leftrightarrow P}$ is the heat flux due to impacting and splashing particles. $\dot{S}_{h,F \leftrightarrow I}$ is the heat flux loss to evaporation. $q(h_{F,s})$ is computed using two predefined heat transfer coefficients, the first between the film and the contaminated surface, and the other, between the film and the internal field. In OpenFOAM (V2 to V6), two models are implemented for the heat flux coefficient, htc. The first allows setting a constant heat transfer coefficient between the liquid film and the contaminated surface. The second allows setting a convective heat transfer coefficient condition between the wall film region and the internal field given by the following equation (NEXTfoam, 2017):

If $Re_F < 5.10^5$

$$htc_p = \frac{0.664 Re_F^{0.5} Pr^{0.333} \kappa_p}{L} \tag{8.a}$$

else

$$htc_p = \frac{0.037 Re_F^{0.8} Pr^{0.333} \kappa_p}{L} \tag{8.b}$$

with $Re_F = L \rho_F |\mathbf{u_F} - \mathbf{u_B}| / \mu_F$, $\mathbf{u_B}$ is the tangential velocity vector at the boundary and L a constant length scale that, according to Incropera et al. (2007), models the flat plate length.

Numerical method

In this CFD study, the heat transfer between a flat plate and a liquid film formed by a spray impingement is investigated. This section presents the general structure of the solver, the numerical schemes discretizing the fields, as well as the boundary conditions.

General solver structure

Most of the computational domain is designed to model the gaseous part of the problem where particles evolve, namely, the internal field. The rest of the domain is defined as a wall film region. This multi-region approach offered by OpenFOAM allows solving different equations in different sets of cells in the same computational domain.

The pressure field is corrected twice. The transient calculations are made with a maximum allowed Courant number CFL_{max} set in the pre-processing phase using an adjusted time step strategy. At each time step, the particle number is computed using the particle number update equation:

$$P_n = P_{n-1} + P_{s,n-1} - P_{a,n-1} + P_{inj,n} \qquad (9)$$

The current particle mass is then computed, resolving the particle evaporation equations. Finally, the particle momentum is calculated solving Newton's second law equation. After resolving all the spray cloud equations (Nobile, 2015), the solver calculates the intersections between the particle trajectories and the thin film. It evaluates $P_{s,n}$ and $P_{a,n}$ for the next time step and resolves the thin film equations. Next, the internal field's density, momentum, species and energy are computed in a PISO loop (Holzmann, 2016b) with a stability criterion of 10^{-5} for $\mathbf{U}$ and h in this study. The pressure is then solved using the geometric algebraic multigrid (GAMG) solver (Greenshields, 2017). The turbulent kinetic energy and dissipation are computed at the end of each time step.

Numerical schemes
Standard numerical schemes OpenFOAM are used to solve the mathematical model. Time derivative terms are computed using an implicit, bounded first-order transient discretization scheme (CFDDirect, 2017). Gradient terms are computed using the second-order Gauss linear scheme. This scheme is based on the Gaussian divergence theorem for the volume integral of a gradient field (Greenshields, 2015; CFDDirect, 2017). It actually specifies a standard finite volume discretization of the Gaussian integration that requires the interpolation of values from the cell centres to the cell face centres. This interpolation scheme is then given by the linear input, which means a linear interpolation or a central differentiation.
The divergence of the velocity $\mathbf{U}$ and the effective shear tensor $\boldsymbol{\tau}_{\mathbf{eff}}$ are both calculated with the same Gauss linear scheme used for the discretization of the gradients, while the rest of divergence terms are computed using a first-order upwind scheme which determines the value of a scalar from the direction of the flow. In this paper, the results (Nusselt distribution) are similar to that which would be obtained with a second-order scheme. In fact, the airflow is not really critical for the Nusselt distribution, but rather, the droplet flow is the main actor. The numerical scheme for the Laplacian calculation is similar to that presented for the gradient. Finally, linear interpolations are used for all calculations.

Boundary and initial conditions
This study examines the radial evolution of the Nusselt number between the liquid film and a contaminated surface. Therefore, the computational domain used in this study is cylindrical. Figure 3 presents the case configuration and the domain mesh. The computational domain dimensions are based on the spray source diameter D = 1cm, with a radius of 7D and a height of 5.5D.
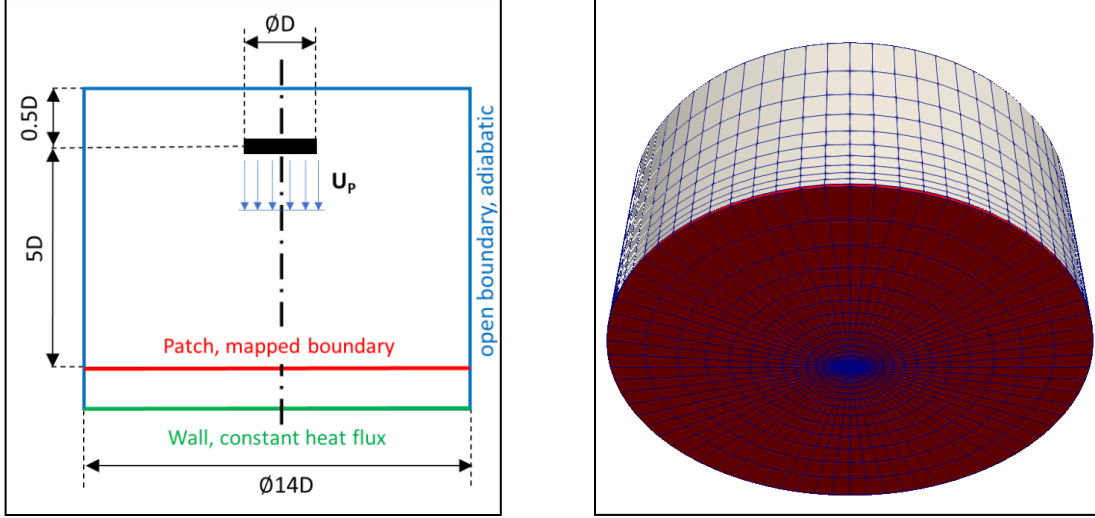
Figure 3: Water spray impingement case configuration (left) and numerical mesh (right)

The spray source is placed at H = 5D from the flat plate. The upper and radial boundaries of the entire domain (blue boundary on the figure) constitute a wave transmissive patch (NEXTfoam, 2017). This boundary condition avoids wave reflections, which allows species to flow in and out of the computation domain freely, depending on flow conditions. A zero-gradient boundary condition is set for temperature. The open boundary corresponds to the real case. The lower boundary is a wall with a constant heat flux of $q_w = 15.10^3 \text{W/m}^2$. This boundary does not reflect the real case, and was only set to compute the Nusselt number and make comparison with (Stevens and Webb, 1991) experimental results. A mapped boundary is set between the wall film region and the internal field to allow the transfer of all source terms presented in the mathematical model. Initially, the domain is set at a cold temperature of $T_0 = 273.15\text{K}$ and the spray is injected at a hot temperature of $T_{P0} = 333.15\text{K}$. 1 million particles per second, with a diameter between 1mm and 8mm, are injected normally into the surface with a velocity magnitude of 1m/s. The spray mass flow rate is 0.04 kg/s.

Thermophysical properties
The internal field is composed of three species. The density ρ, the specific heat capacity c_p and the dynamic viscosity μ are weighted by species mass fraction Y_{specie}. They also vary as a function of the temperature. The density is computed using the perfect gas law (eq. 10.a). The specific heat capacity of each species is computed as a function of the temperature from a set of coefficients taken from JANAF tables of thermodynamics (eq. 10.b). Finally, the dynamic viscosity follows the Sutherland law. The parameter values used in equations 10.a, 10.b and 10.c are presented in Table 1.

$$\rho = \sum_{specie} Y_{specie} \times \frac{M_{specie}}{RT} p \tag{10.a}$$

$$cp = \sum_{specie} Y_{specie} \times \left(\left(\left(a_{4,specie}T + a_{3,specie}\right)T + a_{2,specie}\right)T + a_{1,specie}\right)T + a_{0,specie} \tag{10.b}$$

$$\mu = \frac{As\sqrt{T}}{1 + T_s/T} \tag{10.c}$$

Table 1: Thermophysical parameters

|	M[kg/m³]	A_s[kg/msK⁻¹]	T_s[K]	a_0	a_1	a_2	a_3	a_4
N₂	28.01	1.67×10^{-6}	171	3.3	1.41×10^{-3}	-3.96×10^{-6}	5.64×10^{-9}	-2.44×10^{-12}
O₂	32	1.67×10^{-6}	171	3.21	1.13×10^{-3}	-5.76×10^{-7}	1.31×10^{-9}	-8.77×10^{-13}
H₂O	18.02	1.67×10^{-6}	171	3.39	3.74×10^{-3}	-6.35×10^{-6}	6.97×10^{-9}	-2.51×10^{-12}

For the particles and the liquid film, the density is set to 10^3kg/m^3, $cp = 4.18 \times 10^3 \text{J/kg. K}$, and the Prandtl number is set to 0.7.

Model verification
In this study, the spray is defined as a particle stream. Throughout the simulation, the liquid film is fed by a non-stationary distribution of particles. Therefore, steady state conditions will not be reached. However, the film temperature will reach a certain value and will continue to fluctuate in a narrow range around this value. Here, a "pseudo-steady state" regime is defined when the film temperature reaches this range. In this section, a mesh convergence study is elaborated and the influence of the jet parameter (spray's Reynold Number Re_D, number of particles and mass flow rate) on the Nusselt number Nu_D, film thickness δ_F and film Reynolds number Re_F is presented. To evaluate the influence of the parameters, a temporal average of different quantities (film thickness, velocity, temperature, etc.) in the pseudo-steady state regime is computed.

Mesh dependency study
A grid study is conducted to analyse the effect of the spatial discretization on the solution. The meshes used in this study have a cylindric shape, as presented in Figure 3. The meshes are characterised by the number of cells n_r, n_φ and n_z in the radial, angular and axial directions, respectively. Figure 4 presents a top view ($z = 5.5D$) and an axial section ($y = 0$) of a coarse mesh. The location of the spray source is also presented.
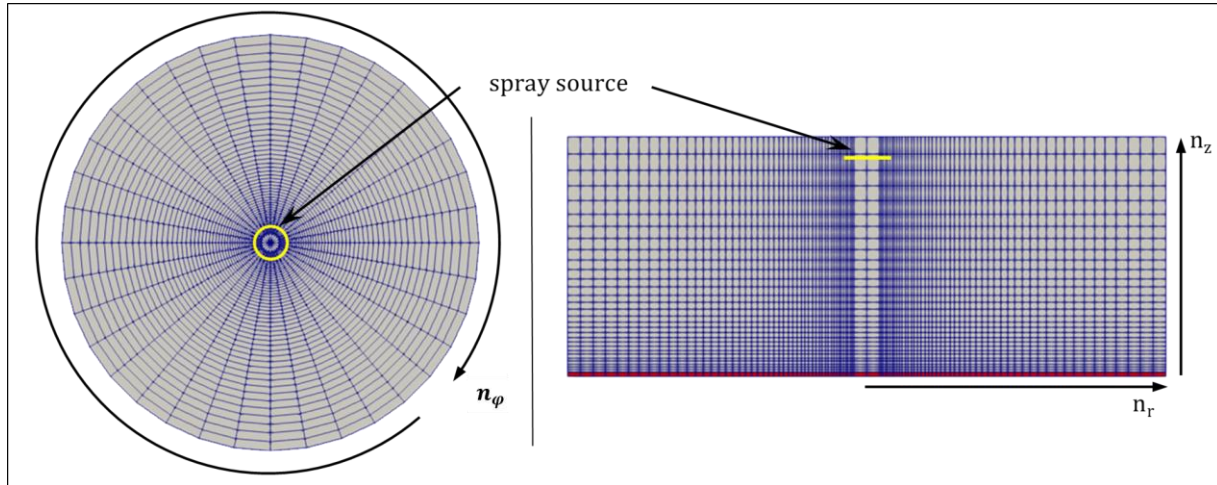
Figure 4: Top view (left) and axial section (right) of the mesh

As presented in Figure 4, refinements are made in the radial and axial directions, and thus, the meshes are finer near the stagnation zone (the area where the jet impacts the wall). Four meshes were tested: a coarse, a normal, a fine, and an extra-fine mesh. Table 2 presents the characteristics of different meshes, and n_{tot} is the total number of cells.

Table 2: Characteristics of different meshes

	Coarse	Normal	Fine	Extra-fine
n_r	42	84	140	210
n_φ	36	72	120	180
n_z	30	60	100	150
n_{tot}	4.54×10^4	3.63×10^5	1.68×10^6	5.67×10^6

Figure 5 shows an axial section of the internal field superimposed on the wall film region (coarse mesh). The difference between the two sides of the figure is that, on the right part, the spray cloud is hidden to display the cells adjacent to particles. For the wall film region and the spray cloud, temperatures are presented (T_P and T_F), and for the internal field, the mass fraction Y_{H_2O} is presented. The temperatures show that the spray and the

film are cooled in the direction of the flow. For the internal field, we notice that the water vapour is concentrated near the stagnation zone, likely due to the gas stagnation in this zone.

Several studies have focused on the film flow created by the interaction of a continuous jet with a wall (Stevens and Webb, 1991; Liu, Gabour and Lienhard, 1993). In those studies, the local Nusselt number Nu_D is expressed as a function of the radial distance from the centre of the stagnation zone. There are many structural differences between a continuous jet and a spray, and as a result, there may also be differences when comparing the heat transfer of both with a wall. However, far from the impingement zone, the heat transfer should depend more on the local thin film properties than on the on the jet properties. Thus, the injection parameters, such as the Reynolds number Re_D and the inclination angle θ, should have similar effects on the heat transfer. For this reason, the Nusselt number is defined as in those experimental studies. At each time step, the film temperature is not necessarily axisymmetric because particle distribution is poly-dispersed, and so heat transfer could vary instantly as a function of the azimuthal angle φ. A mapped Nusselt number $\widetilde{Nu}_D$ is defined here as a function of the radial distance and the azimuthal angle. Equations 11, 12 and 13 present respectively the mapped, local and global Nusselt number.

$$\widetilde{Nu}_D(r,\varphi,t) = \frac{h(r,\varphi,t)D}{\kappa} = \frac{D}{\kappa} \times \frac{q_w}{T_{spray} - T_{Film}(r,\varphi,t)} \tag{11}$$

$$Nu_D(r,t) = \frac{1}{2\pi} \int_{\varphi=0}^{2\pi} \widetilde{Nu}_D(r,\varphi,t)\, d\varphi \tag{12}$$

$$\overline{Nu}_D(t) = \frac{1}{7D} \int_{r=0}^{7D} Nu_D(r,t)\, dr \tag{13}$$
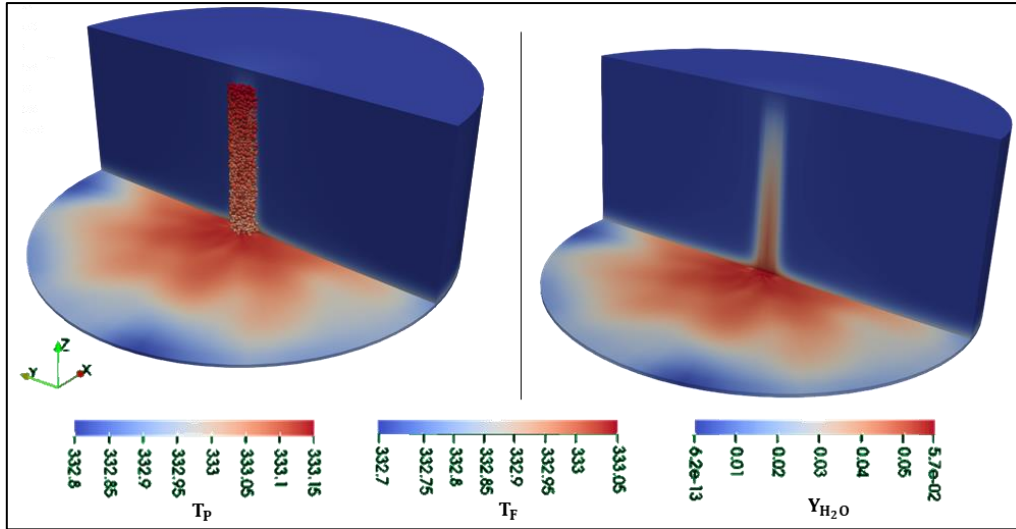

Figure 5: Particle and film temperature and spatial distribution of H$_2$O species

Figure 6 presents the temporal evolution of the global Nusselt number and of the global film thickness. The vertical discontinuous lines mark the time when the film thickness and the Nusselt number reach their average stable values. The film thickness reaches its maximum range before the Nusselt number does. This appears to be logical, as the Nusselt number cannot reach a steady state if the film thickness is still evolving. The first liquid quantity formed in the wall film region is cooled by convection from the internal field. At the second discontinuous line, a hot gas layer in the internal field is fully developed above the wall film region (see Figure 7). Therefore, the pseudo-steady state regime starts when the Nusselt number reaches its average stable value (the second discontinuous line).
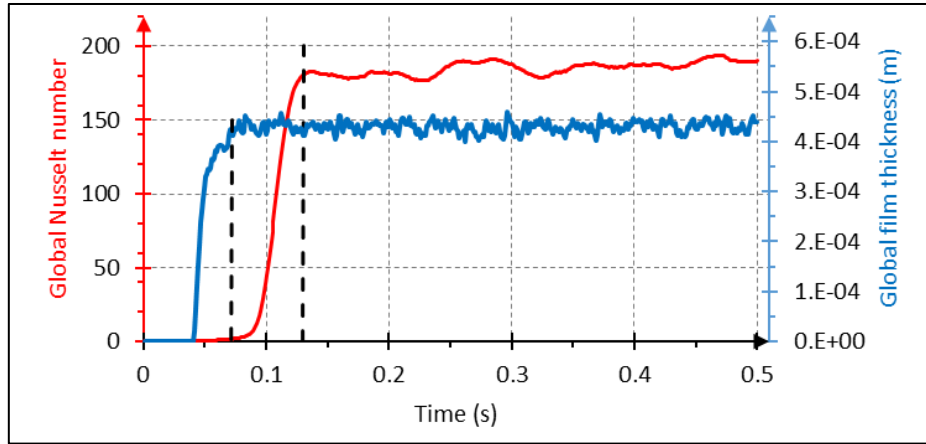
Figure 6: Film thickness (blue) and global Nusselt number (red) evolution
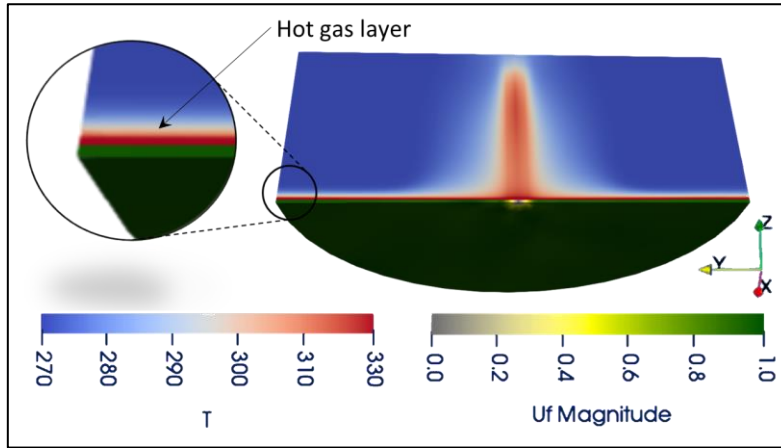
Figure 7: Hot gas layer above the film surface

The local Nusselt number of the pseudo-steady state regime, $Nu_{D,S}$, is defined as a time-averaged function of the local Nusselt number presented in equation 12 from the start point of the pseudo-steady state regime to the simulation end time (0.5 s). The mesh dependency study is based on $Nu_{D,S}$.
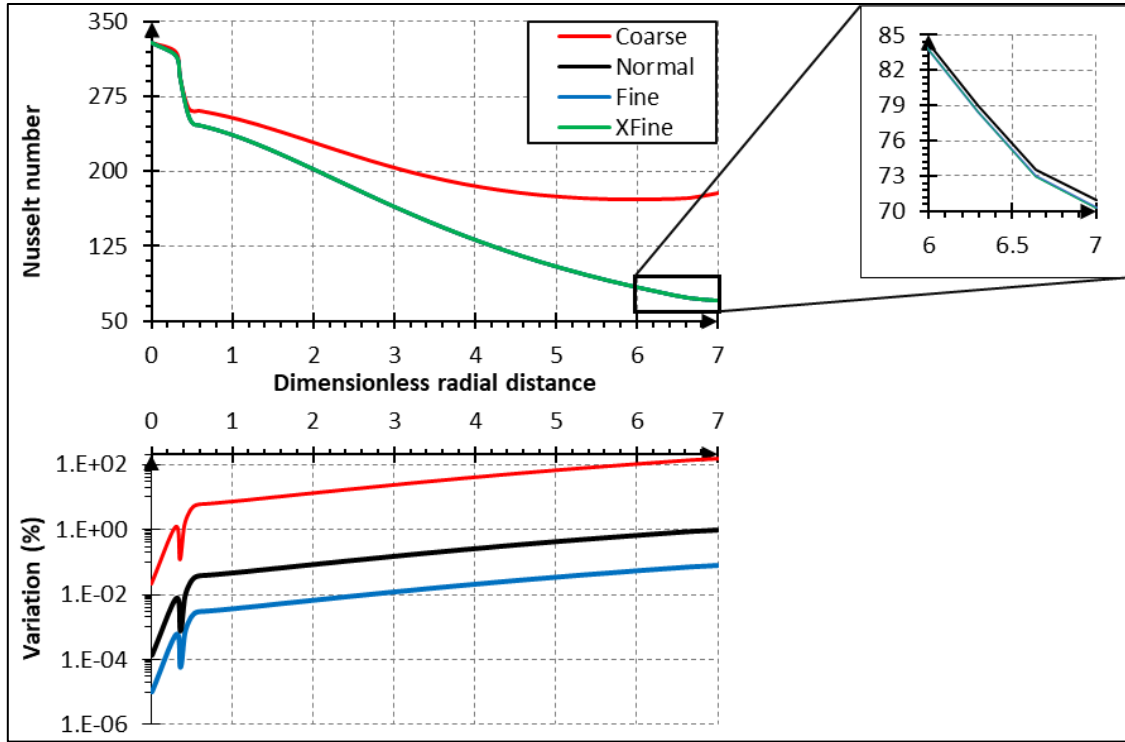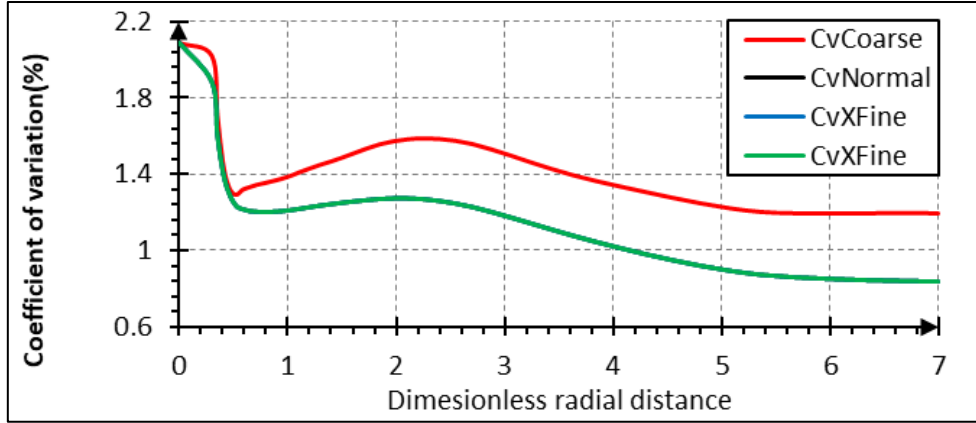
Figure 8: Local Nusselt number of the pseudo-steady state regime distributions and variation for different meshes

Figure 8 presents the radial distribution and variation (based on the extra fine mesh) of the local Nusselt number. The Nusselt number variation is defined in equation 14. For the coarse, normal and fine meshes, the variation increases with radial distance. In the stagnation zone, all the meshes give almost the same Nusselt number value (a variation of less than 1%). The normal mesh has a maximum variation of 1% at $r = 7D$, which makes it acceptable in an engineering context. From this point on, the normal mesh (3.63×10^5 cells) will be used in all simulations.

$$\text{variation}_\%(r) = 100 \times \frac{\left|\text{Nu}_D(r) - \text{Nu}_{D,\text{Xfine}}(r)\right|}{\text{Nu}_{D,\text{Xfine}}(r)} \tag{14}$$

Figure 9 shows the local Nusselt number coefficient of variation in the pseudo-steady state regime. The largest variation is around $(r < D/2)$, where the spray penetrates the film region, then it decreases while departing from the stagnation zone. This could be explained by a homogenization of the film outside of the stagnation zone; film liquid droplets accumulate to form a less turbulent flow. The coefficient of variation for the non-coarse meshes at $r = 7D$ ($\simeq 0.84\%$) shows that the temporal evolution of the heat transfer is almost stabilised. For the coarse mesh, the derivative of the coefficient of variation with respect to the radial position becomes positive at $r = 6$, which could be due to a discretization error, given the large cell size.

Figure 9: Coefficient of variation of the local Nusselt number for different meshes (at pseudo-steady state regime)

This mesh size is considered as a very coarse mesh for numerical models using the volume of fluid approach. Edin and Šefko (2015) used 2.1e5 cells for a two-dimensional control volume (3.7D×12D) with the same software. Having a large cell size (compared to Eulerian methods) that limits the discretization error to less than 1% makes computations on a large computation domain (characteristic of the aircraft ground deicing process) possible, with a reasonable computing cost.

Effect of spray parameter
The spray cloud class implemented in OpenFOAM allows the user to set the mass flow rate $\dot{M}$, the particle's diameter distribution, the particle rate (the number of injected particles per second) $\dot{N}_p$, the particle inlet velocity U_p, and the break-up and atomization models. In the pre-processing phase, a constraint is added to ensure a physical inlet condition.

In this subsection, the effects of the particle inlet velocity (Reynolds number $Re_D = U_p D/\nu$), the mass flow rate and the particle rate are investigated. The Rosin-Rammler distribution implemented in OpenFOAM enables setting the particle diameter range. The particle diameter d_P is calculated with equation 15 using 4 parameters: d_{min}, d_{max} and d_{mean}, respectively the minimum, the maximum and the mean particle diameter to be injected, and n, a distribution parameter.

$$d_P = d_{min} + d_{mean} \times \left[-\ln\left(1 - \Gamma(0,1) \times \left(1 - e^{-\left(\frac{d_{max}-d_{min}}{d_{mean}}\right)^n} \right) \right) \right]^{1/n} \tag{15}$$

where $\Gamma(0,1)$ is the uniform distribution.

The inlet constraint used in this study is presented in equations 16 and 17. First, based on the particle sizes, the particle mean mass is computed using a primary number of particles noted here n_{Data}. n_{Data} should be big enough to let $m_{P.mean}$ converge. In this study, $n_{Data} = 2 \times 10^4$ was used after testing several values.

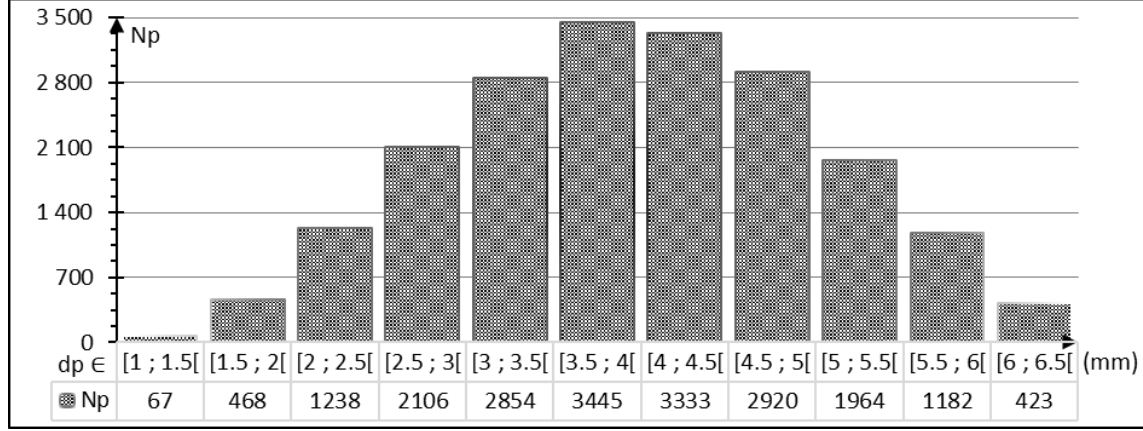$$m_{P.mean} = \frac{1}{n_{Data}} \times \rho_P \frac{\pi}{6} \sum_{i=1}^{n_{Data}} d_p^3 \tag{16}$$

$$N_p = \frac{M}{m_{P.mean}} \tag{17}$$

With this constraint, it is impossible to vary $\dot{M}, \dot{N}_P$ and equation 14 parameters freely. Another constraint (equation 17) on the equation's 14 parameters is added for this study. With this constraint, a change in d_{min} value will modify the whole particle distribution.

$$d_{max} = 8 \cdot d_{min} = \frac{9}{2} \cdot d_{mean} \quad ; \quad n = 3 \tag{18}$$

Figure 10 shows a histogram of the injected particle diameter distribution using a minimum particle diameter of 1mm. A discretization of 0.5mm was performed on the abscissa axis, making the figure readable.

dp ∈	[1 ; 1.5[	[1.5 ; 2[	[2 ; 2.5[	[2.5 ; 3[	[3 ; 3.5[	[3.5 ; 4[	[4 ; 4.5[	[4.5 ; 5[	[5 ; 5.5[	[5.5 ; 6[	[6 ; 6.5[	(mm)
Np	67	468	1238	2106	2854	3445	3333	2920	1964	1182	423	

Figure 10: Histogram of particle diameter distribution ($n_{Data} = 2 \times 10^4$)

The spray inlet conditions for different configuration are summarised in Table 3: 4 Reynolds number values $\left(Re_{i(i\in[\![1,4]\!])}\right)$, 4 particle number rate values $\left(\dot{N}p_{i(i\in[\![1,4]\!])}\right)$ and 4 mass flow rate values $\left(\dot{M}_{i(i\in[\![1,4]\!])}\right)$.

Table 3: Spray inlet conditions for different cases

Configuration	Re_D	$d_{min}(m)$	$\dot{M}(kg/s)$	$\dot{N}p$ (particles/s)
Re_1	10.5e3	1.00e-3	4.00e-2	1.00e6
Re_2	21.1e3	1.00e-3	4.00e-2	1.00e6
Re_3	63.3e3	1.00e-3	4.00e-2	1.00e6
Re_4	105e3	1.00e-3	4.00e-2	1.00e6
$\dot{N}p_1$	21.1e3	2.00e-3	4.00e-2	0.13e6
$\dot{N}p_2$	21.1e3	1.00e-3	4.00e-2	1.00e6
$\dot{N}p_3$	21.1e3	0.50e-3	4.00e-2	8.00e6
$\dot{N}p_4$	21.1e3	0.25e-3	4.00e-2	64.0e6
$\dot{M}_1$	21.1e3	9.11e-4	3.00e-2	1.00e6
$\dot{M}_2$	21.1e3	1.00e-3	4.00e-2	1.00e6
$\dot{M}_3$	21.1e3	1.08e-3	5.00e-2	1.00e6
$\dot{M}_4$	21.1e3	1.15e-3	6.00e-2	1.00e6

Figure 11 presents the local Nusselt number and its coefficient of variation in the pseudo-steady-state regime for the different configurations above. The top line graphs study the Reynolds number effect. The middle line graphs study the particle number rate effect, and the bottom line graphs study the mass flow rate effect.

For a spray, contrary to the continuous jet, the Reynolds number can be increased while keeping the same mass flow rate. The Nusselt number distributions corresponding to a Reynolds number between 10,557 and 63,342 are almost identical (a maximum 4.5% difference at the stagnation zone level). The Nusselt number distribution corresponding to a Reynolds Number of 105,570 is higher. This can be explained by the fact that the high velocity of the injected spray has brought more momentum to the wall film, thus increasing the film velocity. The turbulent heat transfer correlation, Equation 8. b, is therefore used instead of Equation 8. a at the interface between the internal field and the wall film region.

The coefficient of variation increases because the same number of particles is injected while increasing the inlet velocity; this increases the time interval that separates two particles impacting the wall successively.

Conversely, increasing the particle number rate will reduce this separating time interval. This hypothesis is confirmed by the coefficient of variation reduction with the reduced particle number rate $\left(\dot{N}p_{i(i\in[\![1,4]\!])}\right)$.

Experimentally, increasing the Reynolds number has the effect of increasing the heat transfer (Stevens and Webb, 1991). The same effect can be observed by increasing the mass flow rate and the particle number rate. Having the same particle number and increasing the mass confined in each particle leads to a greater heat transfer variation between time steps of the pseudo-steady state regime. This is shown by the coefficient of variation evolution with the mass flow rate $\left(\dot{M}_{i(i\in[\![1,4]\!])}\right)$.

Increasing the spray mass flow rate increases the momentum transferred to the film. However, spraying the same mass with the same inlet velocity while decreasing the droplet size will increase the film momentum, and then, the heat transfer. This observation should be further investigated in order to optimize the aircraft's de-icing process because with the same amount of energy (temperature, mass, inlet velocity), ice can be removed faster.

In all the presented results, the Nusselt number distributions show maximum values in the stagnation zone, followed by an inflection point at $r \simeq D/2$. The same morphology can be observed in many experimental studies (Webb and Ma, 1995), but the inflection point occurs farther downstream on the wall film ($r\approx 2D$). This difference could be due to the convective heat transfer coefficient models situated between the wall film region and the internal field. The model implemented in OpenFOAM is more adapted to the prediction of an average global Nusselt number because the characteristic length L is independent of the radial distance from the stagnation point. This motivates the development of new correlations of the local heat transfer coefficient that take into account the radial distance. For the verification of the two-region model, the equations already implemented in OpenFOAM are deemed sufficient.
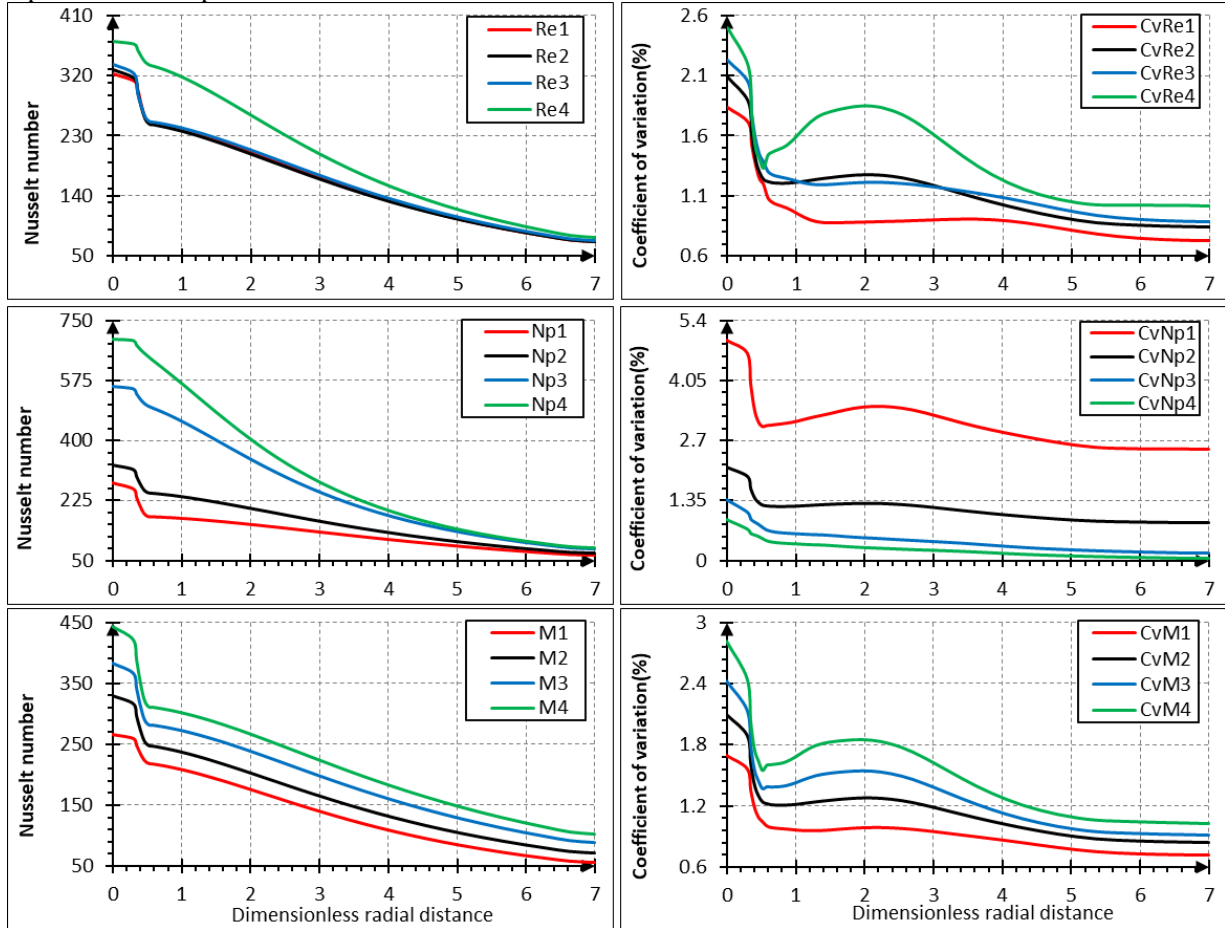
Figure 11: Time-averaged local Nusselt number distribution and coefficient of variation for different spray's inlet condition

Spray penetration

To validate the spray model prior to impact, the spray penetration is studied under non-evaporating chamber conditions. Experimental validation data were taken from Mitroglou et al. (2006). In their experiments, the spray characteristics of a 6-hole injector for a direct-injection gasoline engine were investigated with iso-octane fuel. The methodology used here is inspired from Wang, Ge and Reitz (2010). It consists of a mesh-dependency study of spray tip penetration for 4 injection pressure cases. Details of the case setup are summarised in the table below.

Table 4: case setup

Fuel type	Iso-octane
Nozzle diameter	140 μm
Injection pressure (Pin)	120 bar, 200 bar
Injection duration	1.5 ms
Injection fuel amount	8.08mg for 120 bar injection, 10mg for 200 bar (Wang, Ge and Reitz, 2010)
Chamber gas	Not mentioned, supposed to be N_2 (Wang, Ge and Reitz, 2010)
Chamber pressure (Pb)	1 bar and 12 bar
Bore × stroke	139.7 × 152.4 mm

Three mesh sizes were tested, and details are presented in Table 5. Figure 12 shows the spray penetration for the three meshes and the experimental results for the four injection cases. Results show a relatively good agreement with experimental results. Numerical results for spray penetration are almost linear in the four cases. For the two cases where the chamber pressure (Pb) is 200 bar, experimental results are parabolic, with a discrepancy error of 20% (Pin=200 bar) and 17% (Pin=120 bar). The numerical model behaves better in the case where the chamber pressure is 1 bar, and presents an error around 10%.

Table 5: Characteristics of different meshes

	Mesh 1	Mesh 2	Mesh 3
n_r	10	20	40
n_φ	20	40	80
n_z	20	40	80
n_{tot}	4.00×10^3	3.20×10^4	2.56×10^5
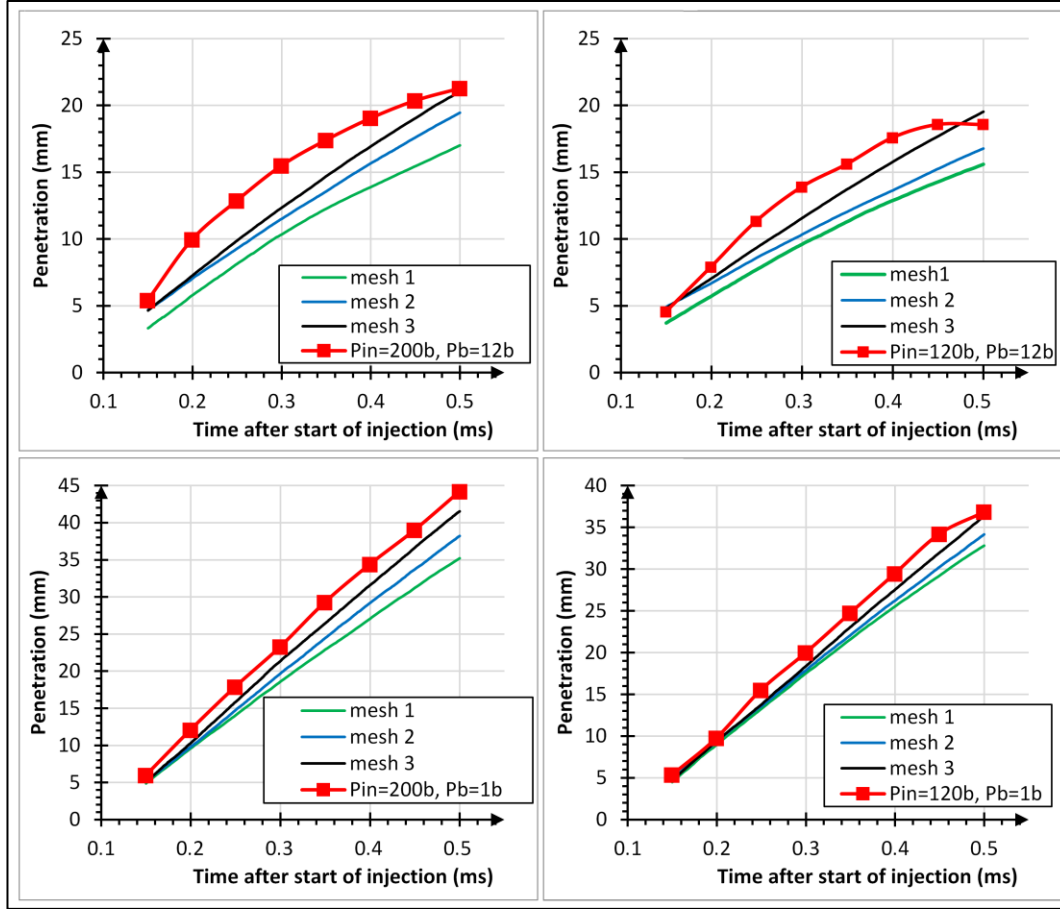
Figure 12: Mesh dependency of liquid penetration compared to experimental results; Left: Pin=200 bar, right: Pin=120 bar, top: Pb=12 bar, bottom: Pb=bar

In the ground deicing process, the spray is injected in a domain with open boundaries and the equivalent chamber pressure is around 1 bar. Consequently, these results are quite satisfactory at this stage.

Heat transfer on flat plate validation
The lack of experimental data relating to heat transfer of an impinging spray on a wall increases the difficulty carrying out a validation. The variation of the heat transfer in this model is sensitive to the momentum transferred to the wall film region. However, keeping the inlet velocity and the mass flow rate constant and modifying the particle number rate while respecting the inlet constraint presented in equations 15 and 16 allows changing the shape of the Nusselt number distribution. On the other hand, Stevens and Webb (1991) investigate the heat transfer caused by the impingement of a continuous jet on a flat plate. In this study, a Reynolds number based on the volume flow rate $\dot{V}$ is suggested $\left(Re_{\dot{V}} = 4\dot{V}/\pi D v\right)$. This definition of the Reynolds number is adapted to the present model as the heat transfer distribution is more sensitive to the volume flow rate than is the inlet velocity. It has been demonstrated in this experimental study that the variation of $Re_{\dot{V}}$ only affects the magnitude of the Nusselt number, i.e., the Nusselt number at the stagnation point (equation 18):

$$Nu_D(r = 0) = A \cdot Re_{\dot{V}}^q \cdot (H/D)^s \cdot (Pr)^{0.4} \tag{19}$$

where A, q and s are correlation parameters depending on the nozzle diameter.

The Reynolds number $Re_{\dot{V}}$ has no effect on the normalised Nusselt number distribution $Nu_D(r)/Nu_D(r = 0)$. Figure 13 presents the experimental results for a nozzle of diameter D=8.9mm against the numerical results presenting the effect of particle number already presented in Figure 11.
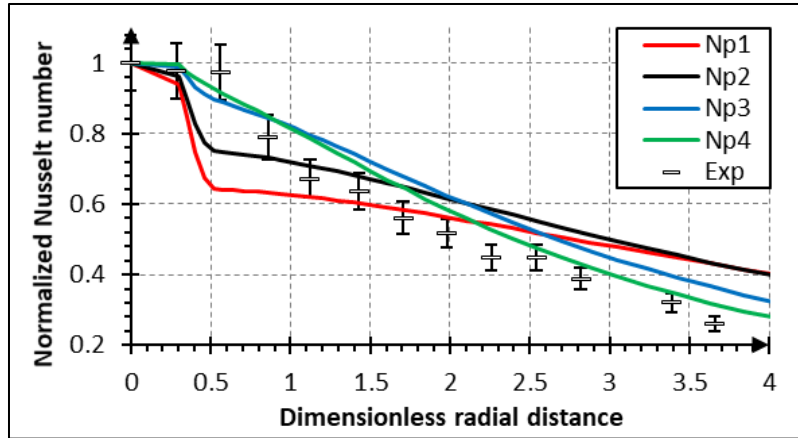
Figure 13: Normalised local Nusselt number distribution (simulation vs experiments)

The discrepancies between the experimental and the numerical results decrease with the particle number rate. The inflection point $(r = D/2)$ in the numerical results disappears for a particle number rate of $3E^6$. A maximum error of 22% was noted for $\dot{N}p = 64e^6$ particles/s. The experimental setup being characterized by an 8% acquisition error, leaves only 14% of error attributable to the difference between the diameter of the nozzles, the distance between the nozzle, and the wall and the particle number rate. This comparison indicates that raising the particle number rate approximates the normalised Nusselt number to that of a continuous jet. This result is important, considering the present state of art, where there is a lack of experimental investigations of the heat transfer of a spray versus many experimental investigations of the heat transfer of a continuous jet. It then provides a method for the validation of numerical models of the same nature as the presented model.

Results and discussion

Inclination angles were studied considering three different angles $(30°, 45°, \text{and } 60°,)$ with the initial and boundary conditions stated in the previous section. The results were compared with the vertical spray. Figure 14 shows the streamlines formed due to the drag force exerted by the gas in the internal field on particles. These streamlines are coloured with particles. The left part of the figure shows that the wall film is warmer in the direction to which the spray is oriented.
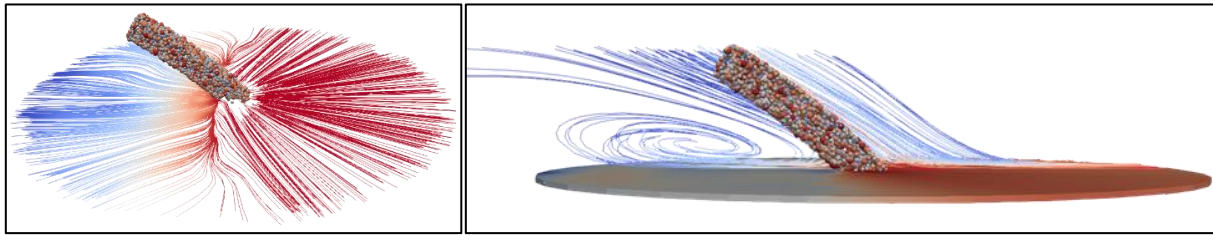
Figure 14: Streamlines of the internal field (θ=30°)

Figure 15 presents the mapped Nusselt number of the pseudo-steady state regime. The mapped Nusselt number characterises the convective heat transfers locally between the liquid film and the wall. The curve set on the left shows the radial distribution of the convective heat transfer in the direction to which the spray is inclined. The curve set on the right shows the angular variation of the mapped Nusselt number at a fixed distance from the stagnation zone $(r = 3D)$. The function $\widetilde{\mathrm{Nu}}_\mathrm{D}(r = 3, \varphi, t) \times \sin(\varphi) = f\left(\widetilde{\mathrm{Nu}}_\mathrm{D}(r = 3, \varphi, t) \times \cos(\varphi)\right)$ is drawn for different inclination angles, i.e. the axes of the second graph are $\widetilde{\mathrm{Nu}}_\mathrm{D}(r = 3, \varphi, t) \times \cos(\varphi)$ for the horizontal axis and $\widetilde{\mathrm{Nu}}_\mathrm{D}(r = 3, \varphi, t) \times \sin(\varphi)$ for the vertical axis. The legend presented is valid for both graphs.
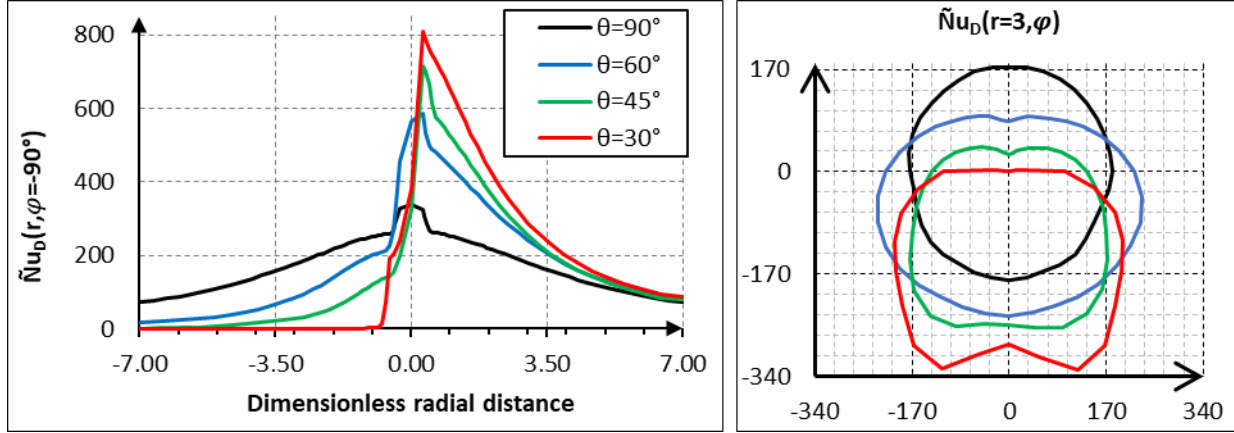
Figure 15: Mapped Nusselt number of the pseudo-steady state regime for different sprays' inclination angles

For the vertical jet, the heat distribution is axisymmetric, as shown by the symmetric curve $(\theta = 90°)$ for the radial distribution and by a circle for the angular distribution. The more the spray is tilted, the more this symmetry is lost. The 30° inclined spray gives a Nusselt number near zero at a distance $r = D$ and in the direction of $\varphi = 90°$, and presents the higher Nusselt number at $\varphi = -90°$. Globally, for the same inlet conditions, the inclination angle increases the maximum Nusselt number by increasing the momentum transferred to the film (locally), and so, it may be more effective to use an inclined spray for a deicing process.

Good ground deicing practice requires avoiding spraying jets perpendicular to a surface to avoid damage to the latter. The CFD model shows that decreasing the inclination angle increases heat transfer, thus potentially accelerating ice melting. The results show that the proposed CFD model can predict the convective heat transfer in the deicing process. Such predictions can help better understand the effect of spray parameters and eventually help reduce ADF volumes used in airports. These results encourage more research effort to develop CFD models dedicated to the aircraft ground deicing simulation. No definitive conclusion can be drawn before the ice region and ice melting are taken into account in the CFD model. Nonetheless, ice is also fragilized by the effect of pressure, but normal pressure decreases with the inclination angle. Parametric studies of the spray, in the context of deicing, should be based on the heat transfer, as well as on the stress tensor transmitted to the ice. The model must then be improved to take into account this interaction. To conclude, the table below summarises the characteristic parameters of the process, the parameters investigated with the proposed model, and indicates whether or not they are critical.

		Table 6: Investigated parameters
Parameter	Investigated values	Critical
Nozzle diameter	Not investigated	-
Nozzle-surface distance	Not investigated	-
Inclination angle	30°, 45°, 60° and 90°	Yes
Reynolds number	10.5e3, 21.1e3, 63.3e3 and 105e3	No significant effect in the range 10e3 to 63e3
Mass rate	3e-2, 4e-2, 5e-2 and 6e-2	Yes

Conclusion

This paper proposes a Eulerian-Lagrangian model that limits the computing costs of scale dispersion problems and enables the investigation by CFD of the influence of an impinging particle spray's parameters on the surface heat transfer. A first region, called the internal field, where particles evolve, cool and evaporate, and a wall film region, where a thin film is formed, both make up the multi-region model. The model is solved within standards libraries of OpenFOAM V6. The domain grid choice is verified. Qualitatively, the model makes good predictions of the effect of the Reynolds number, the particle number rate and the mass flow rate. The spray can be approximated to a continuous liquid jet by increasing the particle number rate, allowing the validation of the

model compared to the experimental studies available. For a spray injection at a pressure of 1 bar, the discrepancies between CFD and experimental results for spray penetrations are below 10%.

Future works will focus on editing the boundary conditions between the internal field and the wall field regions, on validations, and then on adding a third region where ice melt will be modelled. An objective function should also be designed to link heat transfer and surface pressure. A high value for this function must mean good ice decontamination. Such an objective function could serve as a more appropriate basis for comparing deicing scenarios than the Nusselt number. Ice modelling is also mandatory to confirm the present results obtained without ice melting models. The ice shape evolution while melting can indeed affect the liquid film spreading. From a thermal point of view, ice melting cool down the water film. From a geometric point of view, the angle between the spray axis and the ice surface varies with the ice melting, therefore changing the film thickness distribution.

References

Beaugendre, H., Morency, F. and Habashi, W. G. (2006) 'Development of a second generation in-flight icing simulation code', *Journal of Fluids Engineering, American Society of Mechanical Engineers*, 2(128), pp. 378–387. Available at: https://hal.inria.fr/inria-00337571.

Bilodeau, D. R. *et al.* (2016) 'Numerical Modeling of First and Second Order SLD Effects on 3D Geometries', in *8th AIAA Atmospheric and Space Environments Conference*. Reston, Virginia: American Institute of Aeronautics and Astronautics, pp. 1–23. doi: 10.2514/6.2016-3280.

Bourgault, Y. *et al.* (1999) 'A finite element method study of Eulerian droplets impingement models', *International Journal for Numerical Methods in Fluids*, 29(4), pp. 429–449. doi: 10.1002/(SICI)1097-0363(19990228)29:4<429::AID-FLD795>3.0.CO;2-F.

CFDDirect (2017) *OpenFOAM v5 User Guide: 4.4 Numerical schemes*. Available at: https://cfd.direct/openfoam/user-guide/fvschemes/.

Desjardins, O., Moureau, V. and Pitsch, H. (2008) 'An accurate conservative level set/ghost fluid method for simulating turbulent atomization', *Journal of Computational Physics*, 227(18), pp. 8395–8416. doi: 10.1016/j.jcp.2008.05.027.

Durst, F., Milojevic, D. and Schönung, B. (1984) 'Eulerian and Lagrangian predictions of particulate two- phase flows : a numerical study', *Applied Mathematical Modelling*, 8(2), pp. 101–115. doi: 10.1016/0307-904X(84)90062-3.

Edelbauer, W. *et al.* (2016) 'Numerical and experimental investigation of the spray quenching process with an Euler-Eulerian multi-fluid model', *Applied Thermal Engineering*. Elsevier Ltd, 100, pp. 1259–1273. doi: 10.1016/j.applthermaleng.2016.02.131.

Edin, B. and Šefko, Š. (2015) 'Computational Modeling and Simulation of Nonisothermal Free-surface Flow of a Liquid Jet Impinging on a Heated Surface', *Procedia Engineering*. Elsevier B.V., 100, pp. 115–124. doi: 10.1016/j.proeng.2015.01.349.

Fotovat, F., Bi, X. T. and Grace, J. R. (2017) 'Electrostatics in gas-solid fluidized beds: A review', *Chemical Engineering Science*, 173(August), pp. 303–334. doi: 10.1016/j.ces.2017.08.001.

Greenshields, C. J. (2015) 'OpenFOAM programmer's guide v3.0.1', *OpenFOAM Foundation Ltd.*, (December), p. 100.

Greenshields, C. J. (2017) *OpenFOAM User Guide V5*, *OpenFOAM Foundation Ltd*. Available at: http://foam.sourceforge.net/docs/Guides-a4/OpenFOAMUserGuide-A4.pdf.

Habchi, C., Foucart, H. and Baritaud, T. (1999) 'Influence of the wall temperature on the mixture preparation in DI gasoline engines', *Oil and Gas Science and Technology*, 54(2), pp. 211–222. doi: 10.2516/ogst:1999017.

Holzmann, T. (2016a) *Mathematics, Numerics, Derivations and OpenFOAM®*. doi: 10.13140/RG.2.2.27193.36960.

Holzmann, T. (2016b) 'Mathematics, Numerics, Derivations and OpenFOAM', (September), p. 156. doi: 10.13140/RG.2.2.27193.36960.

Incropera, F. P. *et al.* (2007) *Fundamentals of Heat and Mass Transfer*, *US Patent 5,328,671*. doi: 10.1073/pnas.0703993104.

Liu, A. B., Mather, D. and Reitz, R. D. (2010) 'Modeling the Effects of Drop Drag and Breakup on Fuel Sprays', in *SAE Technical Paper Series*. doi: 10.4271/930072.

Liu, X., Gabour, L. A. and Lienhard, J. H. (1993) 'Stagnation-Point Heat Transfer During Impingement of Laminar Liquid Jets: Analysis Including Surface Tension', *Journal of Heat Transfer*, 115(1), p. 99. doi: 10.1115/1.2910677.

Meredith, K. (2010) *Thin Liquid Film Modeling in OpenFOAM*, *5th OpenFOAM Workshop*. Gothenburg, Sweden. Available at: http://web.student.chalmers.se/groups/ofw5/Abstracts/KarlMeredithAbstractOFW5.pdf.

Mitroglou, N. *et al.* (2006) 'Spray characteristics of a multi-hole injector for direct-injection gasoline engines', *International Journal of Engine Research*, 7(3), pp. 255–270. doi: 10.1243/146808705X62922.

Moshansky, T. H. V. P. (1992) *Commission of inquiry into the Air Ontario crash at Dryden, Ontario: Final Report: Technical Appendices*, *Canadian Cataloguing in Publication Data*.

Nasr, G. G., Yule, A. J. and Bendig, L. (2002) *Industrial Sprays and Atomization*. doi: 10.1007/978-1-4471-3816-7.

National Transportation Safety Board (1993) *Aircraft Accident Report Washington, D.C. 20594 AIRCRAFT, Takeoff stall in icing Conditions USAIR flight 405 FOKKER F-28, New York March 22,1992*. Available at: http://www.ntsb.gov/investigations/AccidentReports/Reports/AAR0003.pdf.

NEXTfoam (2017) 'Boundary Conditions - OpenFOAM-4.1', (May), p. 94.

Nobile, M. (2015) *Improvement of Lagrangian approach for multiphase flow*. Göteborg, Suède. Available at: http://www.tfd.chalmers.se/~hani/kurser/OS_CFD_2014/Matteo Nobile/RevisedReport_MatteoNobile.pdf.

Pourbagian, M. and Habashi, W. G. (2015) 'Aero-thermal optimization of in-flight electro-thermal ice protection systems in transient de-icing mode', *International Journal of Heat and Fluid Flow*. Elsevier Inc., 54, pp. 167–182. doi: 10.1016/j.ijheatfluidflow.2015.05.012.

Reid, T. *et al.* (2010) 'FENSAP-ICE: Application of Unsteady CHT to De-Icing Simulations on a Wing with Inter-Cycle Ice Formation', in *AIAA Atmospheric and Space Environments Conference*. Reston, Virigina: American Institute of Aeronautics and Astronautics, pp. 1–11. doi: 10.2514/6.2010-7835.

Shinjo, J. and Umemura, A. (2010) 'Simulation of liquid jet primary breakup: Dynamics of ligament and droplet formation', *International Journal of Multiphase Flow*. Elsevier Ltd, 36(7), pp. 513–532. doi: 10.1016/j.ijmultiphaseflow.2010.03.008.

Stanton, D. W. and Rutland, C. J. (1998) 'Multi-dimensional modeling of thin liquid films and spray-wall interactions resulting from impinging sprays', *International Journal of Heat and Mass Transfer*, 41(20), pp. 3037–3054. doi: 10.1016/S0017-9310(98)00054-4.

Stevens, J. and Webb, B. W. (1991) 'Local Heat Transfer Coefficients Under an Axisymmetric, Single-Phase Liquid Jet', *Journal of Heat Transfer*, 113(1), p. 71. doi: 10.1115/1.2910554.

Stiesch, G. (2003) *Modeling Engine Spray and Combustion Processes*, *Springer-Verlag Berlin Heidelberg*. Berlin, Heidelberg: Springer Berlin Heidelberg (Heat and Mass Transfer). doi: 10.1007/978-3-662-08790-9.

Transport Canada (2005) *Guidelines for Aircraft Ground Icing Operations (Chapter 13)*. Ottawa. Available at: http://www.tc.gc.ca/publications/en/tp14052/pdf/hr/tp14052e.pdf.

Velraj, R. *et al.* (1999) 'HEAT TRANSFER ENHANCEMENT IN A LATENT HEAT STORAGE SYSTEM †', 65(3), pp. 171–180.

Wang, Y., Ge, H.-W. and Reitz, R. D. (2010) 'Validation of Mesh- and Timestep- Independent Spray Models for Multi-Dimensional Engine CFD Simulation', *SAE International Journal of Fuels and Lubricants*, 3(1), pp. 277–302. doi: 10.4271/2010-01-0626.

Webb, B. W. and Ma, C.-F. (1995) 'Single-Phase Liquid Jet Impingement Heat Transfer', *Advances in Heat Transfer*, 26, pp. 105–217. doi: 10.1016/S0065-2717(08)70296-X.

Wong, Jim, Papadakis, M. and Wong, Jon (2013) 'CFD Analysis of a Wing with a Bleed Air Ice Protection System', in *5th AIAA Atmospheric and Space Environments Conference*. Reston, Virginia: American Institute of Aeronautics and Astronautics, pp. 1–26. doi: 10.2514/6.2013-2935.

Yakhya, S., Ernez, S. and Morency, F. (2019) 'Computational Fluid Dynamics Investigation of Transient Effects of Aircraft Ground Deicing Jets', *Journal of Thermophysics and Heat Transfer*, 33(1), pp. 117–127. doi: 10.2514/1.T5428.

Yoon, S. S. *et al.* (2004) 'Numerical modeling and experimental measurements of a high speed solid-cone water spray for use in fire suppression applications', *International Journal of Multiphase Flow*, 30(11), pp. 1369–1388. doi: 10.1016/j.ijmultiphaseflow.2004.07.006.

Zhao, L. *et al.* (2017) 'An Experimental and Numerical Study of Diesel Spray Impingement on a Flat Plate', *SAE International Journal of Fuels and Lubricants*, 10(2), pp. 2017-01–0854. doi: 10.4271/2017-01-0854.

Zhao, L. *et al.* (2018) 'Evaluation of Diesel Spray-Wall Interaction and Morphology around Impingement Location', in *SAE Technical Paper Series*, pp. 1–17. doi: 10.4271/2018-01-0276.